JOURNAL OF APPLIED CRYSTALLOGRAPHY

ISSN: 1600-5767
journals.iucr.org/j

Removing multiple outliers and single-crystal artefacts from X-ray diffraction computed tomography data

Antonios Vamvakeros, Simon D. M. Jacques, Marco Di Michiel, Vesna Middelkoop, Christopher K. Egan, Robert J. Cernik and Andrew M. Beale

J. Appl. Cryst. (2015). **48**, 1943–1955

JOURNAL OF APPLIED CRYSTALLOGRAPHY
ISSN 1600-5767

Removing multiple outliers and single-crystal artefacts from X-ray diffraction computed tomography data

Antonios Vamvakeros,[a,b]* Simon D. M. Jacques,[a,b,c]* Marco Di Michiel,[d] Vesna Middelkoop,[e] Christopher K. Egan,[c] Robert J. Cernik[c] and Andrew M. Beale[a,b]*

[a]Department of Chemistry, University College London, 20 Gordon Street, London WC1H 0AJ, England, [b]UK Catalysis Hub, Research Complex at Harwell, Didcot, Oxfordshire, England, [c]School of Materials, University of Manchester, Manchester M13 9PL, England, [d]ESRF, The European Synchrotron, Grenoble, F-38000, France, and [e]Flemish Institute for Technological Research, VITO NV, Boeretang 200, Mol, Belgium. *Correspondence e-mail: antonyvam@gmail.com, simon.jacques@gmail.com, andrew.beale@ucl.ac.uk

Received 4 September 2015
Accepted 1 November 2015

Edited by A. Borbély, Ecole National Supérieure des Mines, Saint-Etienne, France

Keywords: XRD-CT; diffraction tomography; powder X-ray diffraction; diffraction images.

Supporting information: this article has supporting information at journals.iucr.org/j

This paper reports a simple but effective filtering approach to deal with single-crystal artefacts in X-ray diffraction computed tomography (XRD-CT). In XRD-CT, large crystallites can produce spots on top of the powder diffraction rings, which, after azimuthal integration and tomographic reconstruction, lead to line/streak artefacts in the tomograms. In the simple approach presented here, the polar transform is taken of collected two-dimensional diffraction patterns followed by directional median/mean filtering prior to integration. Reconstruction of one-dimensional diffraction projection data sets treated in such a way leads to a very significant improvement in reconstructed image quality for systems that exhibit powder spottiness arising from large crystallites. This approach is not computationally heavy which is an important consideration with big data sets such as is the case with XRD-CT. The method should have application to two-dimensional X-ray diffraction data in general where such spottiness arises.

1. Introduction

X-ray diffraction computed tomography (XRD-CT) marries traditional computed tomography with conventional powder X-ray diffraction, offering a powerful chemical imaging method (Hounsfield, 1973; Elliott & Dover, 1982; Harding *et al.*, 1987). It was first demonstrated using laboratory X-ray radiation, but its potential has been more fully realized using synchrotron radiation (Bleuet *et al.*, 2008). Local diffraction signals can be extracted that allow not only the observation and identification of materials that conventional methods such as powder XRD may be blind to, but also the extraction of local chemical and physical information (Egan *et al.*, 2013; Vamvakeros *et al.*, 2015). Obtaining this spatially resolved information is essential in materials science. For example, the distribution of different crystallographic phases and/or elements in a heterogeneous catalyst is expected to directly affect its performance (Grunwaldt *et al.*, 2013; Beale, Jacques *et al.*, 2014). One can readily make the argument that such methods will become standard methods to characterize materials, like conventional X-ray imaging (μCT) and classical *in situ* X-ray powder diffraction. Indeed, this is reflected in the increasing popularity of XRD-CT, and there are now a number of material studies and developmental publications in this area (Stock *et al.*, 2008; Álvarez-Murga *et al.*, 2011; De Nolf & Janssens, 2010; Palancher *et al.*, 2011; Valentini *et al.*, 2011, 2012; Stock & Almer, 2012; Voltolini *et al.*, 2013; Egan *et*

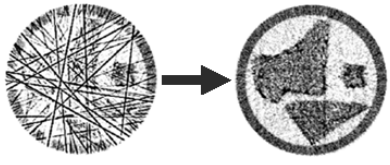

al., 2013; Bonnin *et al.*, 2014; Cedola *et al.*, 2014; Jensen *et al.*, 2015; Vanmeert *et al.*, 2015). Especially in the field of heterogeneous catalysis, XRD-CT has already proven to be a powerful characterization tool used for spatially resolved studies as it allows catalytic reactors to be studied intact and under real process conditions (Jacques *et al.*, 2011; O'Brien *et al.*, 2012; Beale, Gibson *et al.*, 2014; Price *et al.*, 2015; Vamvakeros *et al.*, 2015).

Despite this interest, there are several issues that need to be addressed before the technique can be more widely adopted, and these are mostly associated with treatment and processing of collected data. Included in this are problems associated with crystallite size of materials composing the scanned object. The issue of small crystallites leading to the loss of Bragg diffraction has been addressed by the development of pair distribution function computed tomography, but, to date, there is no adequate procedure for dealing with or preventing the artefacts caused by large crystallites (Jacques *et al.*, 2013). The problem faced becomes a greater issue with higher-resolution XRD-CT scans, where the use of smaller beams can lead to substantial deviations from the ideal powder condition.

1.1. The XRD-CT method

Before elaborating further on this specific problem and the attempts to date to address this, we briefly describe the XRD-CT principle and experiment (see Fig. S1 in the supporting information). The method relies on a pencil-beam scanning approach using a highly collimated or focused monochromatic beam with, for best counting statistics/speed, scattered X-rays recorded on an area detector. This is typically normal to and centred with respect to the beam. If the object under study behaves as a powder, the images obtained will be two-dimensional powder patterns containing powder diffraction rings. Each pattern contains the integral diffraction contributions seen by the detector from the entire length of the beam, so for a 5 mm-diameter sample centred on the beam, ignoring the air scatter from outside the sample, the detector will see diffraction contributions from the entire 5 mm length the beam passes through.

There are several existing approaches to the collection but in all cases the translational scan should be of sufficient size that the object is totally scanned for all measured angles. In many cases though, one may need to perform a translational scan smaller than the cross section of the sample (*e.g.* avoid scanning the whole *in situ* cell in the case of a fixed-bed reactor). However, this means that the diffracting/scattering contribution from these parts of the sample cannot be easily separated/removed from the acquired data. Regarding the angular scan, in most cases it is sufficient to scan angles from 0 to π.

The raw data are thus a four-dimensional projection data set of size $n \times m \times p \times q$ where n is translational sampling, m is rotational sampling and $p \times q$ is the area detector size. As in the case of first-generation X-ray computed tomography, according to the Nyquist sampling theorem, the number of angles scanned should be equal to the number of translational measurements times $\pi/2$ (*i.e.* $m = n \times \pi/2$). However, in practice, the number of angular steps can be decreased without significant changes in the quality of the collected data (Álvarez-Murga *et al.*, 2012). Most typically, the raw four-dimensional data set is reduced by azimuthal integration such that diffraction intensity is stored as a three-dimensional projection data set of size $n \times m \times r$ where r is the number of radial steps, and this third dimension represents the scattering angle 2θ. Features can be extracted from the projection data set and reconstructed to real-space images (of size $n \times n$) using filtered back-projection or algebraic reconstruction methods (Gordon *et al.*, 1970; Kak, 1979). An alternative approach, termed *the reverse analysis method*, is to reconstruct each of the r sinograms to real-space images to produce an $n \times n \times r$ image set which represents reconstructed diffraction patterns for all of the pixels in the measured slice (Bleuet *et al.*, 2008).

1.2. The single-crystal artefact problem

For objects composed of small, randomly orientated crystals the projected diffraction patterns contain 'powder' rings. Where the crystal size is large with respect to the size of the incident beam this moves towards a more single-crystal behaviour and spots appear in the recorded diffraction patterns (Wilchinsky, 1951). This phenomenon is well under-

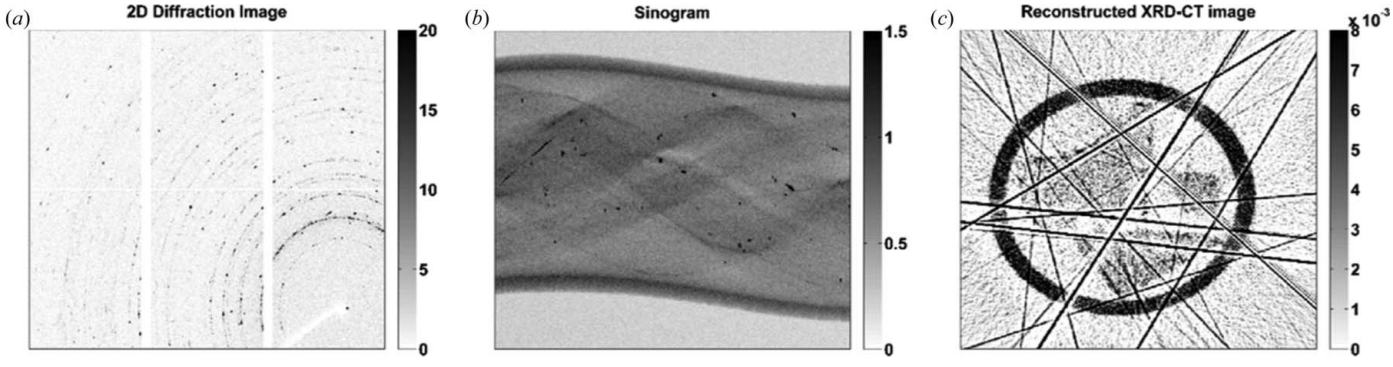

Figure 1
(*a*) A raw two-dimensional diffraction image of 2%La–2%Mn–1.6%Na–3.1%W/SiO_2 catalyst collected during an XRD-CT scan using a 46 keV monochromatic pencil beam with a spot size of 2.5 × 2.5 µm. (*b*) Sinogram of scattering angle 5.3° 2θ corresponding to an SiO_2 cristobalite peak. (*c*) The respective reconstructed XRD-CT image using the filtered back-projection algorithm.

stood but it is important to highlight some points. By large crystallites, here we mean those that represent a large number of repeat crystallographic units. As such, they tend to give rise to strong diffraction signals when lying in a position to satisfy the Bragg condition, leading to high-intensity spots on the detector.

When the incident X-ray beam is small, there are a smaller number of crystallites in the diffracting volume and as such a larger number of spots appear in the recorded diffraction pattern. More specifically, the spottiness arises from the strong diffraction of favoured orientations and is accentuated by a lower population of crystallites which are, by statistical consequence, less randomly orientated. As a result, the diffraction signal generated by each sample volume element (voxel) consists of two components: one that is independent of the voxel orientation (*i.e.* signal produced by the small crystallites randomly orientated) and one that is dependent on the orientation (*i.e.* signal produced by the large crystallites). Fig. 1(*a*) shows an example of a two-dimensional diffraction image exhibiting such spottiness. When radially integrating spotty powder patterns, the integral intensity can deviate significantly from that which would arise from an ideal powder sample.

This can be further exacerbated in XRD-CT where, by the nature of the tomographic collection procedure, the orientation of the studied object favours the measurement of some planes at the expense of others. XRD-CT produces artefact-free images only when the scattering power of every scanned sample volume element (voxel) is independent of the sample orientation. If this condition is not met, then the spotty powder patterns will cause spottiness within the sinogram constructions, as is shown in Fig. 1(*b*), leading to streak artefacts in the reconstructed images, as is shown in Fig. 1(*c*). This phenomenon can be a major problem in XRD-CT data as, if the artefacts are severe, the desired spatial information will be lost.

1.3. Existing strategies for treatment of single-crystal diffraction artefacts

The ideal filter would remove the spots from the raw powder diffraction images while maintaining the intensities of the powder diffraction rings. In XRD-CT, a good approach to mitigate the spottiness problem is to use a continuous-angle scanning approach. Here, the data collection is conducted so that the object is rotated at fixed speed about the tomographic axis and diffraction patterns are accumulated over a fixed angular range (equivalent to the angular step in a stop–start approach). This means that during collection crystallites are swept into the diffracting volume and their orientations are constantly changed and, with respect to the axis of rotation, all angles are equally sampled. This requires continuous rotation in the range 0 to $\sim\pi$ for each translation. Whilst continuous scanning does not necessarily fully eradicate the streak artefact problem, in practice this is the best approach if circumstances permit. However, there are collection strategies and measurement constraints that preclude such measurement and for such one must look for other ways to deal with spotty data.

A simple approach to deal with spottiness is to apply image filtering techniques to the recorded two-dimensional diffraction images (Álvarez-Murga *et al.*, 2012). An image threshold approach has been previously proposed and generally applied in the past. In this method, the pixels that have intensities above the threshold value are excluded in the azimuthal integration (Hammersley, 1998). It is important to note here that replacing pixels above the threshold value with zero should be avoided as this would certainly lead to distortion of Bragg intensity after azimuthal integration. The image threshold approach has also been implemented in recently developed software programs [*GSAS-II* (Toby & Von Dreele, 2013), *XRDUA* (De Nolf *et al.*, 2014), *DAWN* (Basham *et al.*, 2015) and *PyFAI (*Ashiotis *et al.*, 2015)]. Unfortunately, there are potential problems with this approach. Firstly, the threshold is arbitrary since it must be chosen by the user; for individual or a small number of diffraction patterns a 'satisfactory' result can be obtained by eye but for XRD-CT where the data sets can contain several thousand images it would be obviously unrealistic to check each treated image. One could use a harsh threshold to be fairly confident that spots at a specific 2θ angle were removed but this brings us to a second problem: harsh thresholds reduce acquisition statistics. Finally, such methods do not deal with relative difference in intensities at different 2θ values: both strong and weak diffraction peaks may exhibit spottiness and obviously a single threshold cannot deal with this and preserve the required information.

Voltolini *et al.* (2013) also reported the limitations of the threshold method to remove spottiness from the raw two-dimensional diffraction images collected during an XRD-CT experiment. The authors proposed a different approach where the contributions from single crystals and powder are separated in XRD-CT data. This is achieved by (i) applying a median filter for each angle projection set, (ii) subtracting the filtered images from the raw two-dimensional diffraction images to get a spot pattern, (iii) creating masks by setting a threshold using the difference images (involving some image dilation), (iv) removing diffraction spots from the raw diffraction images using the masks, (v) replacing the spots in the raw diffraction images with values from the median filtered images (it is claimed that this is better than replacing with zero values), and (vi) subtracting the images created in step (v) from the raw diffraction images to obtain the large grain images. This approach has some advantages as it is possible to obtain information about the signal generated from both the large crystallites and the powder. Nevertheless, this method is computationally heavy, the image dilation in step (iii) does not guarantee complete removal of the spots and the powder intensities are not maintained because the intensities are based on in-filled values.

Another potential approach is to apply image filtering techniques directly to the sinogram after azimuthal integration. However, in our experience, standard one-dimensional or two-dimensional median filtering is often not effective at removing these artefacts and leads to loss/blurring of information. A better approach may be to employ a sinusoidal median filter specifically designed for sinogram treatment, but

this has yet to be investigated. This is probably not worthwhile, however, as again the median will lead to blurring, though at least in a desired direction.

A different way to deal with streak artefacts in the reconstructed XRD-CT images is to use a method sometimes applied in conventional X-ray tomography (Kak & Slaney, 1988). The intersection of the streaks in the reconstructed images is first found and segmented. This segmented image is then forward-projected to arrive at a sinogram which is then subtracted from the original sinogram. This updated sinogram is then back-projected to arrive, hopefully, at a streak-free image. Although this is a tried and tested method, it requires several computational steps and may not be easily automated or practicable for XRD-CT data.

Herein, we report an alternative approach, which requires minimum user input, to deal with multiple outliers and spottiness in two-dimensional diffraction images. We compare the effect of different filters applied directly to the raw two-dimensional diffraction images collected during XRD-CT experiments. Data from two experiments studying the *in situ* chemistry of working catalytic reactors are presented, one with the use of a monochromatic pencil beam with a spot size of 25 × 25 µm and one with a spot size of 2.5 × 2.5 µm, demonstrating the efficacy of this simple filtering approach even with high-resolution XRD-CT data. This is important as the assumption of an ideal powder can become less valid with decreasing beam size relative to the average crystallite size of the sample, thus leading to spotty diffraction images.

2. Experimental details

Two different catalytic reactors were tested at station ID15A of the ESRF. In each case, the reactor was mounted into a gas delivery stub, itself mounted to a standard goniometer. The goniometer was fixed to a rotation stage set upon a translation stage to facilitate the movements required for the CT measurement. Heating was achieved by virtue of two hot air blowers heating each side of the catalytic membrane reactor. A state-of-the-art PILATUS3 X CdTe 300K hybrid photon-counting area detector, which uses cadmium telluride (CdTe) as the semiconducting direct conversion layer, was used to record the two-dimensional diffraction patterns. Tomographic reconstruction was performed using filtered back-projection (FBP). The MATLAB (The MathWorks Inc., Natick, MA, USA) scripts used in this work are provided in the supporting information. Copies of the radially integrated XRD-CT data after applying the various filters can be found at http://tiny.cc/C5CC03208C.

The first reactor tested was a catalytic membrane reactor (CMR) for the oxidative coupling of methane (OCM) to produce C2 molecules. The 2%Mn–1.6%Na–3.1%W/SiO_2 catalyst bed was packed inside a $BaCo_{0.4}Fe_{0.4}Zr_{0.2}O_{3-\delta}$ (BCFZ) hollow-fibre membrane (2.4 mm diameter and 180 µm wall thickness). The catalyst bed was supported with glass wool. Details of the preparation of catalyst and membranes are given in the supporting information. XRD-CT measurements were performed using a 93 keV monochromatic pencil beam with a spot size of 25 × 25 µm. The XRD-CT measurements were made with 140 translations over 180° in 1.8° steps covering a physical area of 3.5 × 3.5 mm. Reconstruction of these data yielded XRD-CT images with 140 × 140 pixels and 25 µm resolution.

The second reactor was a fixed-bed reactor consisting of a 2%La–2%Mn–1.6%Na–3.1%W/SiO_2 catalyst bed supported with glass wool. Details of the catalyst preparation are given in the supporting information. XRD-CT measurements were performed using a 46 keV monochromatic pencil beam with a spot size of 2.5 × 2.5 µm. The XRD-CT measurements were made with 300 translations over 180° in 0.75° steps covering a physical area of 750 × 750 µm. Reconstruction of these data yielded XRD-CT images with 300 × 300 pixels and 2.5 µm resolution.

3. Results and discussion

We propose a simple method that treats the original two-dimensional diffraction data collected from an XRD-CT experiment (*e.g.* Fig. 2*a*). Firstly, the raw two-dimensional diffraction images are polar transformed to arrive at images illustrated in Fig. 2(*b*). In the polar-transformed image, there are zero elements which were generated as a result of binning the data because only part of the powder diffraction rings were collected (*i.e.* azimuthal range smaller than 0 to 2π). A mask has to be applied to set the values of these pixels to NaN (not a number) values so that these elements are not taken into account during the image reconstruction process. The mask can be created by using either a two-dimensional diffraction image acquired by testing a standard (*e.g.* CeO_2 NIST standard) or any two-dimensional diffraction image acquired during the actual XRD-CT experiment. The pixels with zero intensity generated by binning the data have to be separated from the pixels with zero intensity in the raw two-dimensional images. This is done by (*a*) setting the value of the pixels in the raw two-dimensional image that have zero intensity to an arbitrary positive value (*e.g.* one), (*b*) performing the polar transformation, and (*c*) setting the zero values to NaN and the rest to one. In cases where there are pixels in the raw two-dimensional images with negative or extreme values, these are set to zero before the polar transformation and are then converted to NaN values. The mask that was created for processing the XRD-CT data is presented in Fig. 2(*c*).

It is important to note that this mask needs to be created only once per XRD-CT experiment; it does not require any user input and is then used for processing all the raw two-dimensional diffraction data. More specifically, this is done by multiplying the polar-transformed image with the binary mask (*i.e.* a mask that contains ones and NaN values) and the mean value for each row can be calculated (the MATLAB code developed in-house uses the 'nanmean' function which excludes the NaN values), which generates a vector that represents the respective one-dimensional diffraction pattern (Fig. 2*d*). Note, this process yields the same one-dimensional diffraction patterns as the standard azimuthal integration and

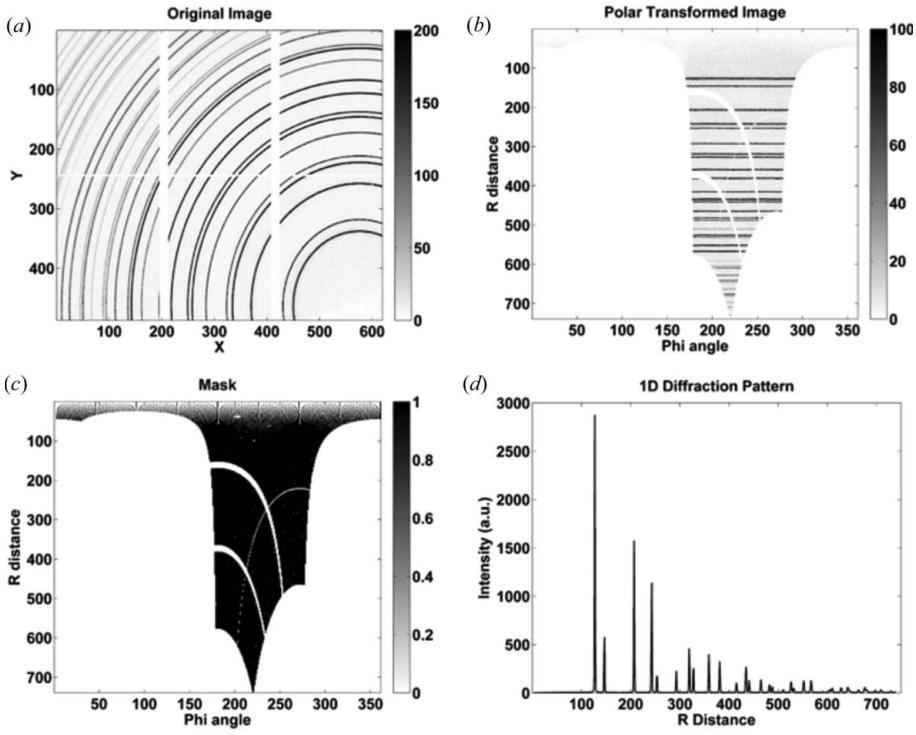

Figure 2
(*a*) Original two-dimensional diffraction data of CeO_2 standard. (*b*) The transformed image in polar coordinates. (*c*) The binary mask containing ones and NaN values. (*d*) The derived one-dimensional diffraction pattern is a vector whose elements are the mean values of each row in the polar-transformed image after the application of the mask.

is also computationally cost equivalent to standard azimuthal integration.

In our recent study, we showed that the crystalline phases present in the 2%Mn–1.6%Na–3.1%W/SiO_2 catalyst at ambient conditions are Na_2WO_4, Mn_2O_3, SiO_2 cristobalite and SiO_2 tridymite (Vamvakeros *et al.*, 2015). We also reported a chemical interaction between the catalyst particles and the BCFZ membrane at the high temperatures required for the OCM reaction, which led to the formation of a new stable phase, identified as $BaWO_4$. This solid-state chemical interaction is a thermal effect as it takes place during temperature ramping without the presence of any reactive gases (*i.e.* before switching to OCM conditions). Unfortunately, the formation of $BaWO_4$ leads also to the formation of large crystallites, themselves giving rise to single-crystal-like diffraction and therefore spottiness in the raw two-dimensional diffraction images. On the other hand, these XRD-CT data present a great opportunity to investigate the effect of different filters during the image reconstruction process. Furthermore, the quality of the sinograms and the reconstructed XRD-CT images corresponding to $BaWO_4$ can serve as a benchmarking tool for the different filters.

In this study, we are presenting the results from a high-temperature XRD-CT scan of the CMR (1048 K). The sinograms being presented here are derived from the highest intensity peaks of SiO_2 cristobalite, $BaWO_4$ and Mn_2O_3 phases. More specifically, these sinograms correspond to scattering angles 1.87, 2.26 and 2.80° 2θ, respectively (Fig. S2). Regarding the BCFZ sinograms, the intensity of the 111 reflection is used (scattering angle 3.22° 2θ). In all the figures

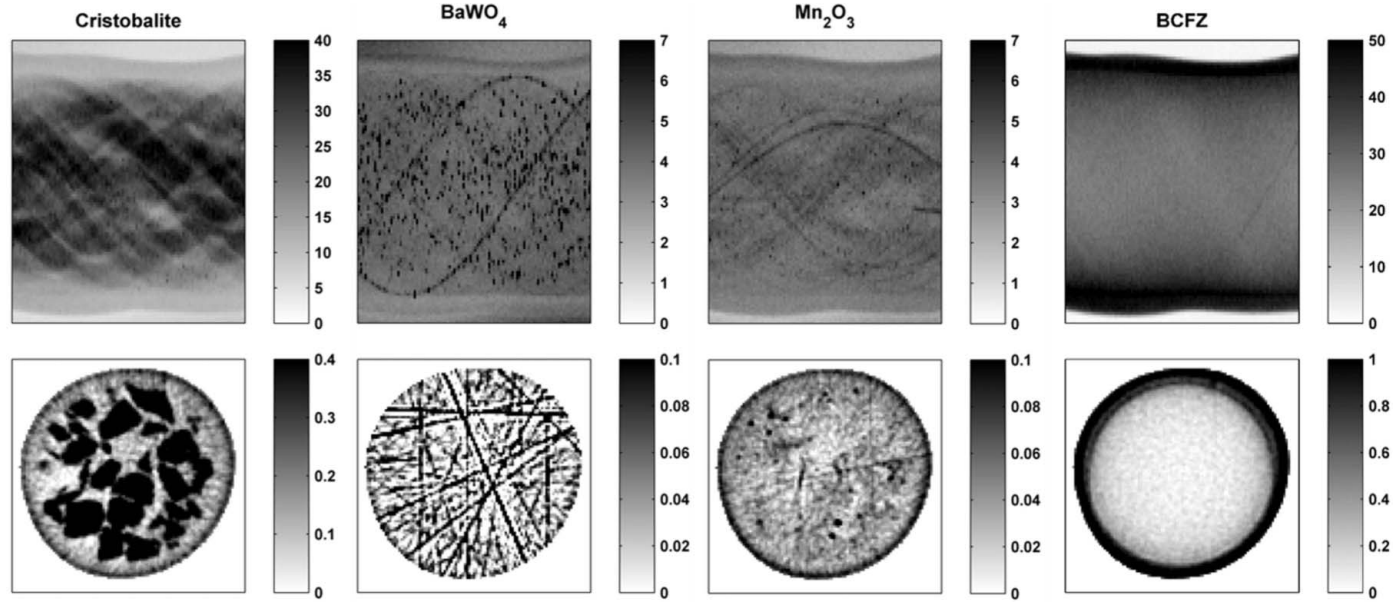

Figure 3
The sinograms of SiO_2 cristobalite, $BaWO_4$, Mn_2O_3 and BCFZ and the corresponding reconstructed XRD-CT images are shown when no filter is used (*i.e.* equivalent to standard azimuthal integration).

presented in this section, a mask has been applied to the reconstructed XRD-CT images, setting the value of the pixels outside the sample to zero.

As mentioned previously, when no filter is applied (*i.e.* equivalent to standard azimuthal integration), the spottiness in the original two-dimensional diffraction images is not suppressed and the reconstructed XRD-CT images contain streak artefacts. In the case of the XRD-CT data presented here, it can be seen in Fig. 3 that the reconstructed image corresponding to the $BaWO_4$ phase is full of streak artefacts and useful information cannot be readily extracted concerning this phase. These artefacts are present to a lesser extent in the image corresponding to the Mn_2O_3 phase and are absent in the images corresponding to the cristobalite and BCFZ phases. Fig. 3 is the template that should be used to compare and assess the effectiveness of the different filters presented in this study. At this point, it should be noted that different reconstruction algorithms (*i.e.* apart from FBP) have also been implemented but the line artefacts remain in the reconstructed images (Fig. S3). As a result, in this study, the FBP algorithm was chosen to reconstruct the sinograms after applying the various filters in the polar-transformed images as it is a very fast and easy-to-implement algorithm.

The advantage of using the polar-transformed images to apply potential filters instead of the raw two-dimensional diffraction images is that a variety of different matrix operations can be easily performed to treat the spottiness. Several different approaches are discussed in the following sections.

3.1. Median filter

The simplest operation that can be applied is a row-wise median operation. The median value of each row is calculated, which is different from the application of a standard median filter to the polar-transformed image. Essentially, this means that the values of each row are sorted and the middle value of the population is stored in a vector. The results are presented in Fig. 4. The streak artefacts are indeed removed but this process leads to distorted images due to the crude nature of this filtering operation.

3.2. Alpha-trimmed-mean filter

Another approach is to apply an alpha-trimmed mean to each row of the polar-transformed image (Bednar & Watt, 1984). The user is requested to provide a percentage for the trimmed mean. This percentage corresponds to a specific number of pixels p for each row in the polar-transformed images. The number p is row dependent as a different number of pixels describe different diffraction peaks in the two-dimensional diffraction images. The values of each row in the polar-transformed images are then sorted and the mean value of each row is calculated after excluding the p pixels. The extreme values are removed from both the high and low end ($p/2$ values, respectively) for every row of the polar-transformed images and reliable intensities without significant loss of information can be obtained. This is shown in Fig. S4 of the supporting information, where the CeO_2 one-dimensional diffraction pattern has been calculated using different values for the alpha-trimmed-mean filter. It is essential to note here that the desired filter should avoid significant decrease in intensity in the obtained one-dimensional diffraction patterns as this would directly alter the chemical information. Although phase distribution maps can still be created when loss of intensity takes place, this should be prevented. If the XRD-CT data are of high enough quality, then sequential whole powder pattern fitting can be performed to create maps showing the change of unit-cell parameters, average crystallite

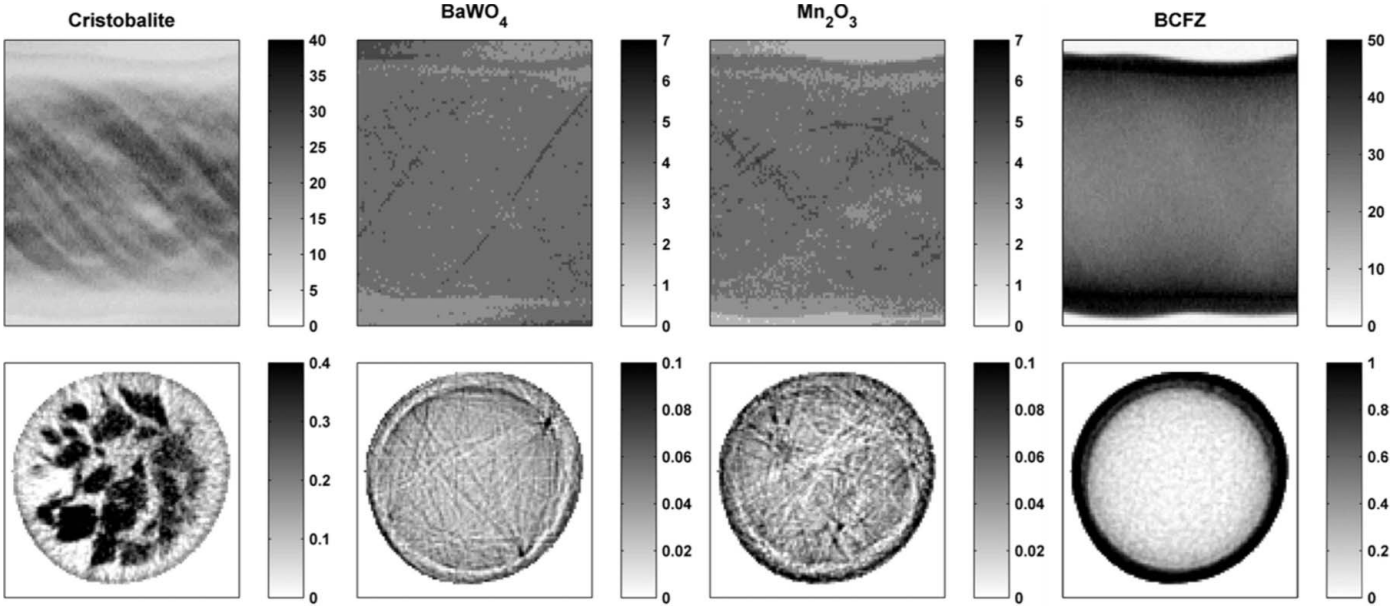

Figure 4
The sinograms of SiO_2 cristobalite, $BaWO_4$, Mn_2O_3 and BCFZ and the corresponding reconstructed XRD-CT images are shown when the median value of each row in the polar-transformed images is used.

size and, in the case of preferred orientation, texture distribution maps (Egan *et al.*, 2013). However, reliable intensities are needed if sequential/parametric Rietveld refinement is to be performed. Therefore, the desired filter should be able to remove outliers and deal with single-crystal diffraction artefacts but at the same time not radically alter the intensities of the other peaks in the derived one-dimensional diffraction patterns.

The effect of the alpha-trimmed-mean filters using different percentages (*i.e.* 0, 1, 2 and 3%) is shown in Fig. 5, where the sinograms and respective images corresponding to $BaWO_4$ are presented; the reason for this choice of display is that the impact of the filters can be readily observed. Indeed, it is impressive that only a 2% trimmed mean is enough to eradicate most of the hotspots in the sinogram while maintaining the main features. The new reconstructed image now reveals the important spatial information that could not be extracted before: the formation of $BaWO_4$ takes place at the interface between the catalyst particles and the inner side of the BCFZ membrane. The effect of a 5, 10, 25 and 50% alpha-trimmed-mean filter has also been investigated but the quality of the reconstructed XRD-CT images does not further improve or deteriorate compared to the 3% alpha-trimmed-mean filter; therefore these results are not presented here.

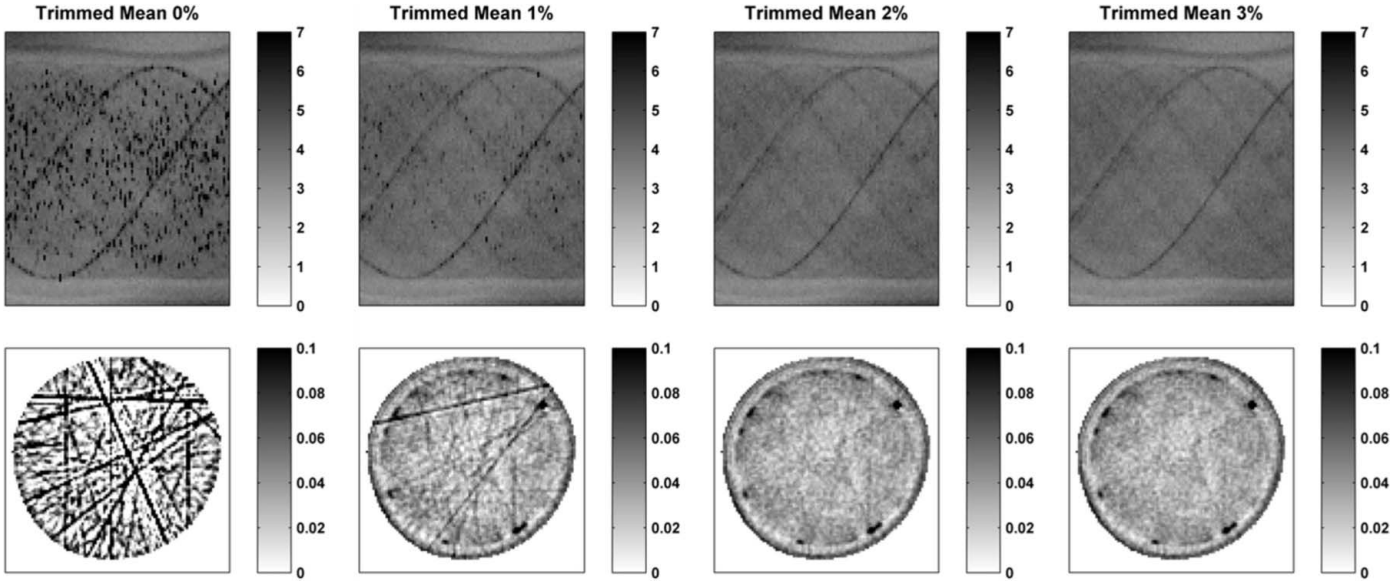

Figure 5
The effect of alpha-trimmed-mean filters using different percentages (*i.e.* 0, 1, 2 and 3%) is shown. The sinograms and respective images correspond to the $BaWO_4$ phase.

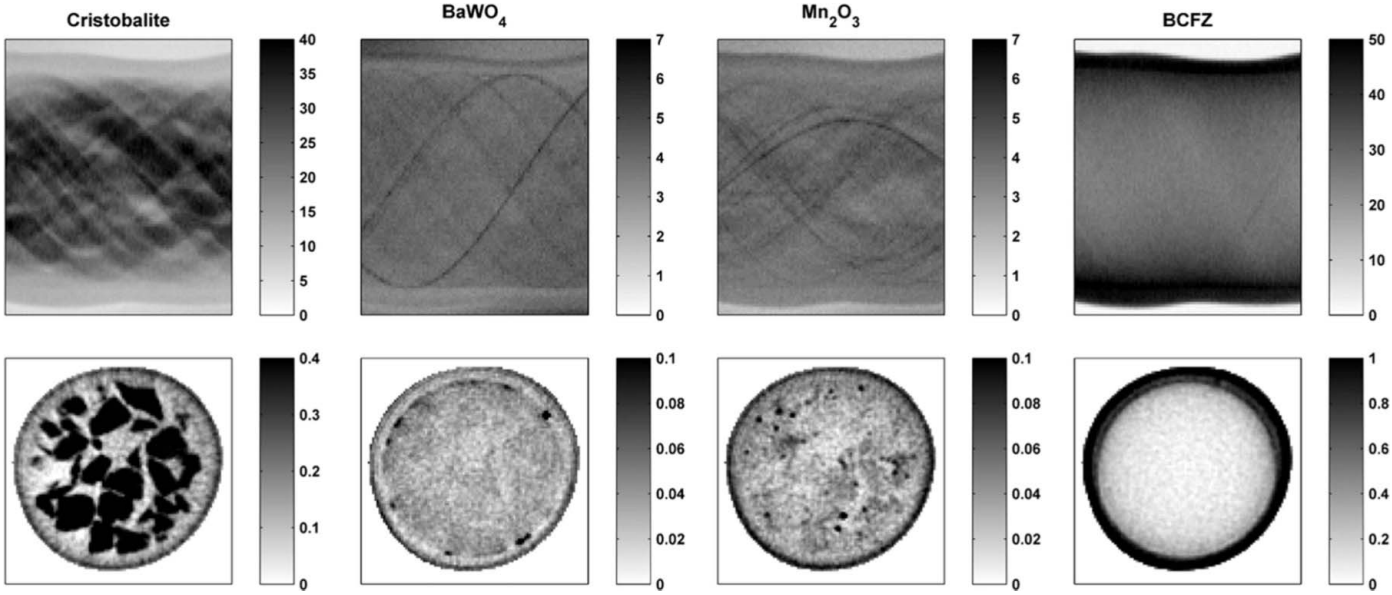

Figure 6
The sinograms of SiO_2 cristobalite, $BaWO_4$, Mn_2O_3 and BCFZ and the corresponding reconstructed XRD-CT images are shown when the 3% alpha-trimmed-mean filter is used.

In Fig. 6, the effect of the 3% trimmed-mean filter is shown. It is important to note that this filter not only removed the artefacts from the $BaWO_4$ XRD-CT image but also improved the quality of the reconstructed images corresponding to the other phases. This improvement is also observable in the Mn_2O_3 XRD-CT image where minor streak artefacts have been removed, yielding a clearer image.

3.3. Standard deviation based trimmed-mean filter

A similar approach to the alpha-trimmed-mean one is the application of a trimmed mean that trims values based on the calculated value of the standard deviation of each row in the polar-transformed images. It works as follows: the absolute value of the difference between the intensity of every pixel of each row and the mean intensity of that row is calculated. If this calculated value is higher than the value of the standard deviation of that row, then the intensity of the pixels that satisfy this condition is set to the NaN value. By replacing the values of these pixels with NaNs, these pixels do not contribute to the statistical result. This means that this filter works in a similar way to an alpha-trimmed-mean filter as it removes pixels from both the high and low end (*i.e.* due to the presence

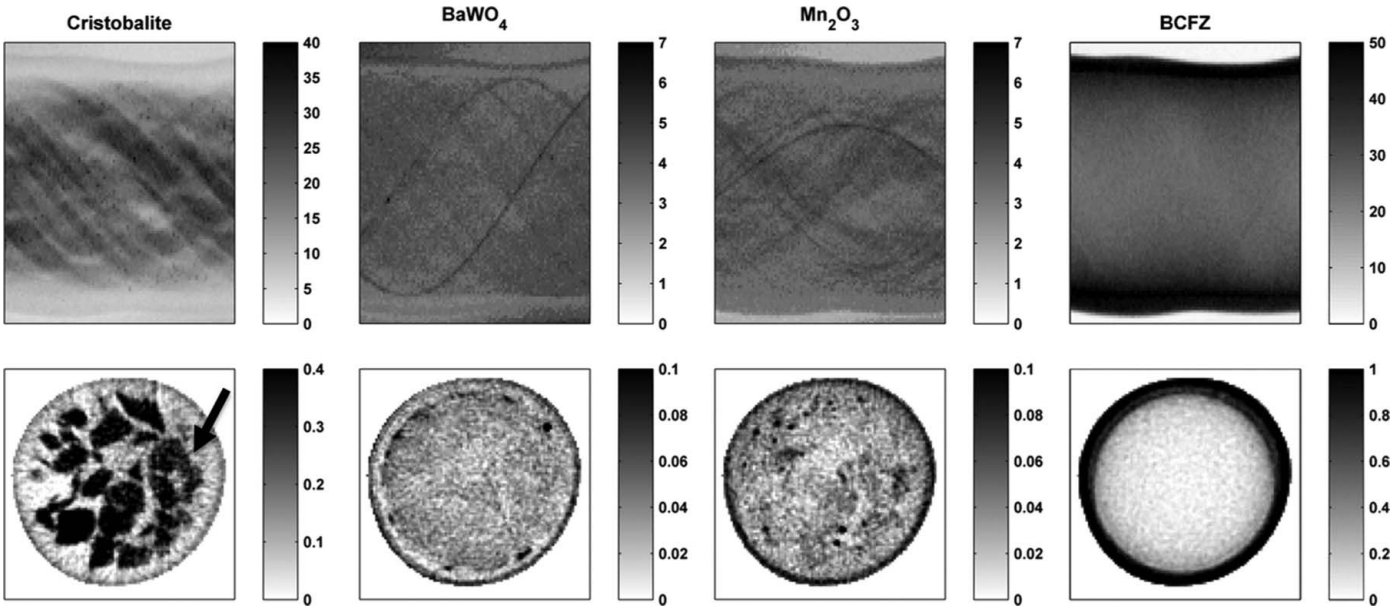

Figure 7
The sinograms of SiO_2 cristobalite, $BaWO_4$, Mn_2O_3 and BCFZ and the corresponding reconstructed XRD-CT images are shown when the SDTM filter, using one standard deviation, is applied.

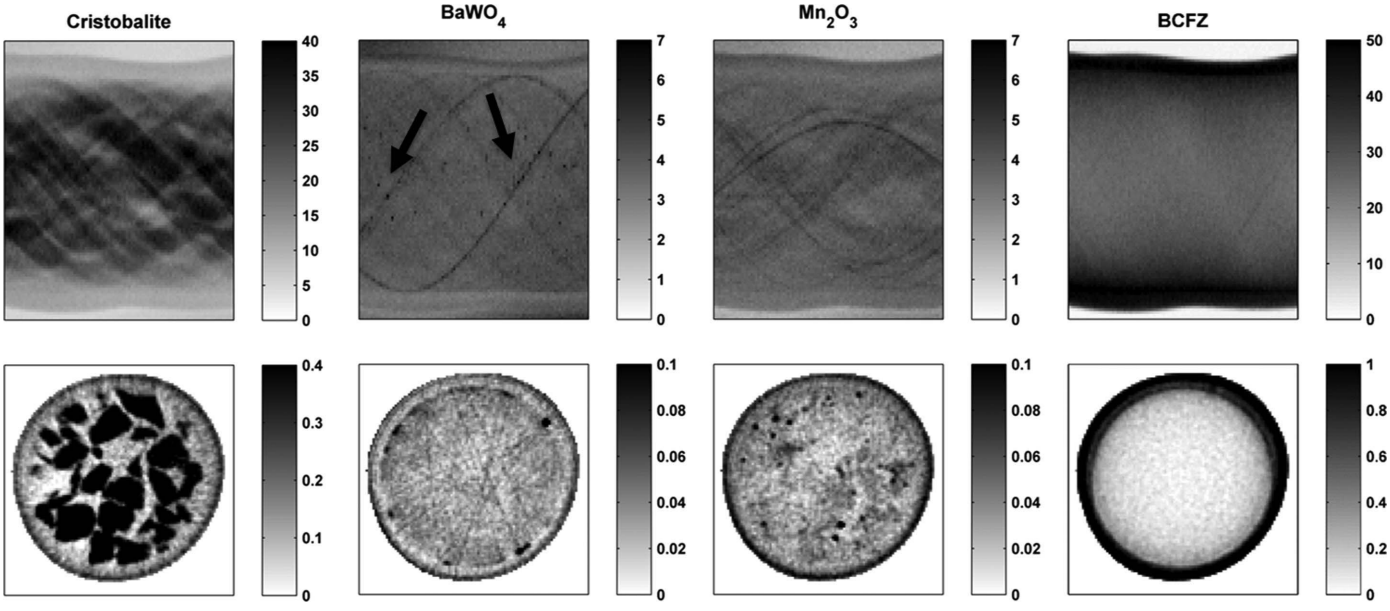

Figure 8
The sinograms of SiO_2 cristobalite, $BaWO_4$, Mn_2O_3 and BCFZ and the corresponding reconstructed XRD-CT images are shown when the SDTM filter, using three times the standard deviation, is applied.

of the absolute in the previous condition). However, in the case of the standard deviation based trimmed-mean (SDTM) filter, the number of elements excluded in each row of the polar-transformed images is not a fixed number but depends on the value of the standard deviation of each row. The user has to specify how many times the standard deviation should be selected as the criterion for the filter to operate.

The effect of the adaptive trimmed-mean filter using one and three times the standard deviation is shown in Figs. 7 and 8, respectively. Where one standard deviation has been applied, most of the artefacts have been removed from the $BaWO_4$ XRD-CT image (Fig. 7). However, there is loss of intensity in the cristobalite phase, as highlighted by the arrow in Fig. 7. On the other hand, when using three standard deviations, it is shown that the intensity of the cristobalite XRD-CT image is maintained but there are still streak artefacts in the $BaWO_4$ XRD-CT image (Fig. 8). This can also be observed by inspecting the $BaWO_4$ sinogram where a significant number of hotspots have not been removed, as highlighted by the arrows in Fig. 8. The behaviour of this filter can be rationalized as follows: when there are spotty powder diffraction rings in the raw two-dimensional diffraction images, the value of the calculated standard deviation for the respective row in the polar-transformed image can be high enough that not enough pixels are rejected during filtering. Similarly, in cases where the calculated standard deviation is too low, a significant number of pixels may end up being rejected. An alternative approach to the SDTM filter would be to perform the trimming based on a more robust statistical measure, like the median absolute deviation (MAD) estimator, similar to the Hampel identifier, instead of the value of the standard deviation for each row of the polar-transformed images (Davies & Gather, 1993). The Hampel identifier is used to identify outliers, which may not be appropriate in the case of very spotty two-dimensional diffraction images, but this remains to be investigated. Unfortunately, it also requires the user to choose a threshold value.

3.4. Two-dimensional order statistic median filters

Finally, an alternative method to deal with spottiness in the raw two-dimensional diffraction images is to apply local order statistic filters to the polar-transformed images (Bovik *et al.*, 1983). The three filters presented here are *n*th rank-order filters (Nodes & Gallagher, 1982). This local filtering process requires a few extra steps as certain software programs may not be able to handle correctly the NaN values present in the polar-transformed images after the application of the binary mask (Fig. 2*c*). For example, the developed MATLAB in-house script uses the 'ordfilt2' function that allows the user to create custom two-dimensional order statistic filters but fails if there are NaN values present in the image to be processed. Fortunately, there is a quick way to overcome this problem. For every row in the polar-transformed images, the pixels that have NaN values are moved to the end of the row (Fig. 9*a*). It is important to note here that this matrix operation is not equivalent to sorting the values because the application of a filter (*e.g.* local median filter) to a row with sorted values will radically alter the results. The next step is to create another binary image containing ones and NaN values which will be used as a mask later on (Fig. 9*b*). Finally, the NaN values in the transformed image are set to zero, the desired filter is applied to the transformed image and the new image is multiplied with the new mask. As before, the respective one-dimensional diffraction pattern is a vector whose elements are the mean values of each row (Fig. 9*c*). Also it should be noted that these local filters can be combined very easily with the ones previously mentioned in this study (*e.g.* first apply the local median filter and then a trimmed-mean filter).

The effect of local median filters is shown in Fig. 10, where the sinograms and respective images corresponding to $BaWO_4$ are presented. A simple filter that can be applied is the traditional median filter where the domain of operation is a three-by-three matrix (*i.e.* eight neighbouring pixels). As can be seen in Fig. 10, although most of the hotspots have been removed in the sinograms, not all have been eradicated, which leads to the formation of a few streak artefacts in the reconstructed images. The next filter is a cross median filter where the domain of operation is again a three-by-three matrix but only the north, east, west and south neighbouring pixels are taken into account. This filter eradicates the hotspots in the sinogram but at the expense of losing intensity, which can be easily observed in the respective reconstructed image. Last but

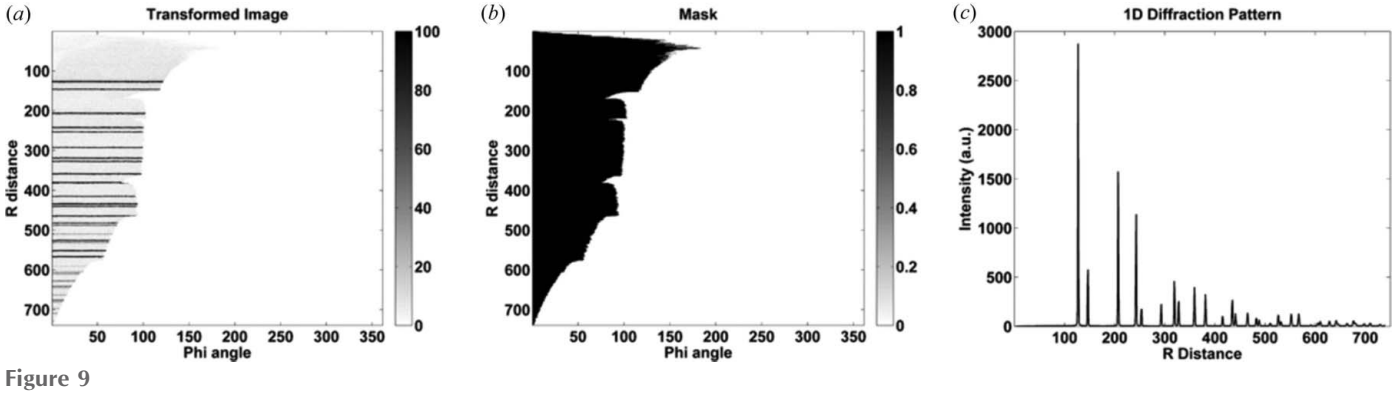

Figure 9
(*a*) The transformed image in polar coordinates. (*b*) The binary mask containing ones and NaN values. (*c*) The derived one-dimensional diffraction pattern is a vector whose elements are the mean values of each row in the polar-transformed image after the application of the mask. The two-dimensional diffraction image using the CeO_2 presented in Fig. 2 is used.

not least, a median row filter [1 1 1 1 1] is applied which blurs information only in the horizontal direction. The domain of operation for this filter is a five-by-one matrix where the first and second, east and west, neighbouring pixels are taken into account. This filter shows promising results as it eradicates the hotspots in the sinogram without any significant loss of intensity.

In Fig. 11, the effect of the median row filter [1 1 1 1 1] is illustrated. It shows that this filter not only eradicated the artefacts associated with the $BaWO_4$ images but also improved the Mn_2O_3 images. Unfortunately, there is loss of intensity in the SiO_2 cristobalite images (*i.e.* both in the sinogram and in the corresponding reconstructed image as highlighted by the arrow in Fig. 11) compared to images created with standard azimuthal integration (Fig. 3) and the 3% trimmed-mean filter (Fig. 6).

3.5. High-resolution XRD-CT data

The results from a high-resolution XRD-CT scan of a 2%La–2%Mn–1.6%Na–3.1%W/SiO_2 catalyst at ambient conditions are shown in Fig. 12. The sinograms being presented here are derived from raw scattering intensity of SiO_2 cristobalite, SiO_2 tridymite, SiO_2 quartz and Na_2WO_4

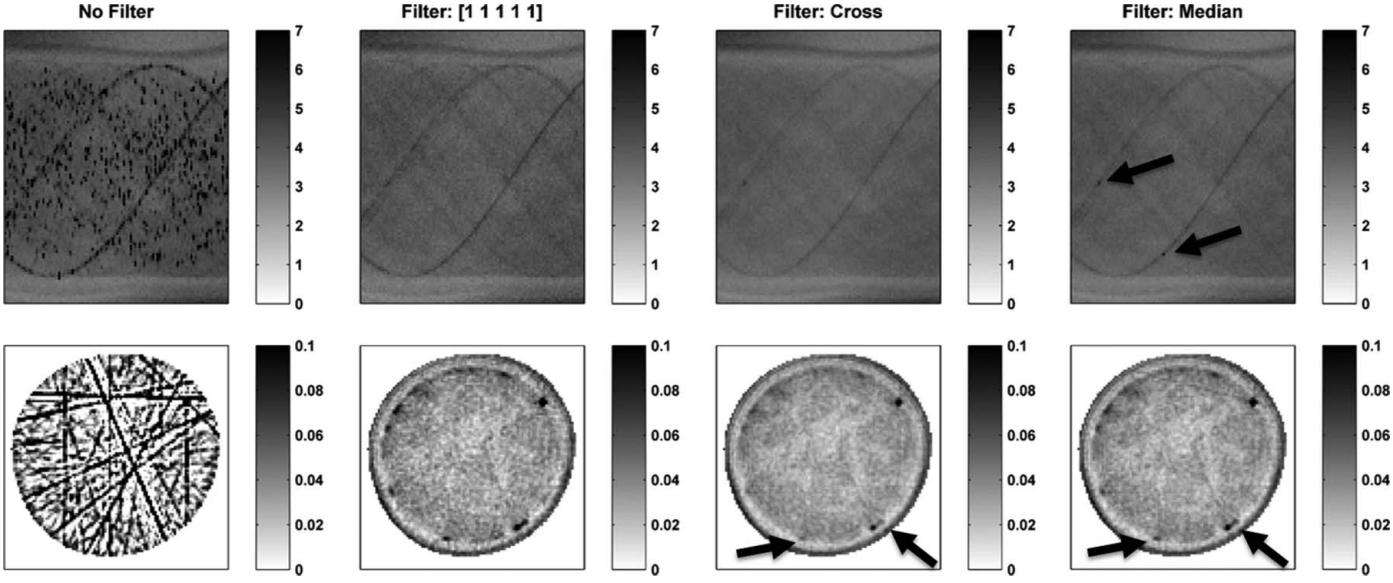

Figure 10
The effect of different local median filters (*i.e.* a 1 × 5 row, a cross and a 3 × 3 median filter) is shown. The sinograms and respective reconstructed images correspond to the $BaWO_4$ phase.

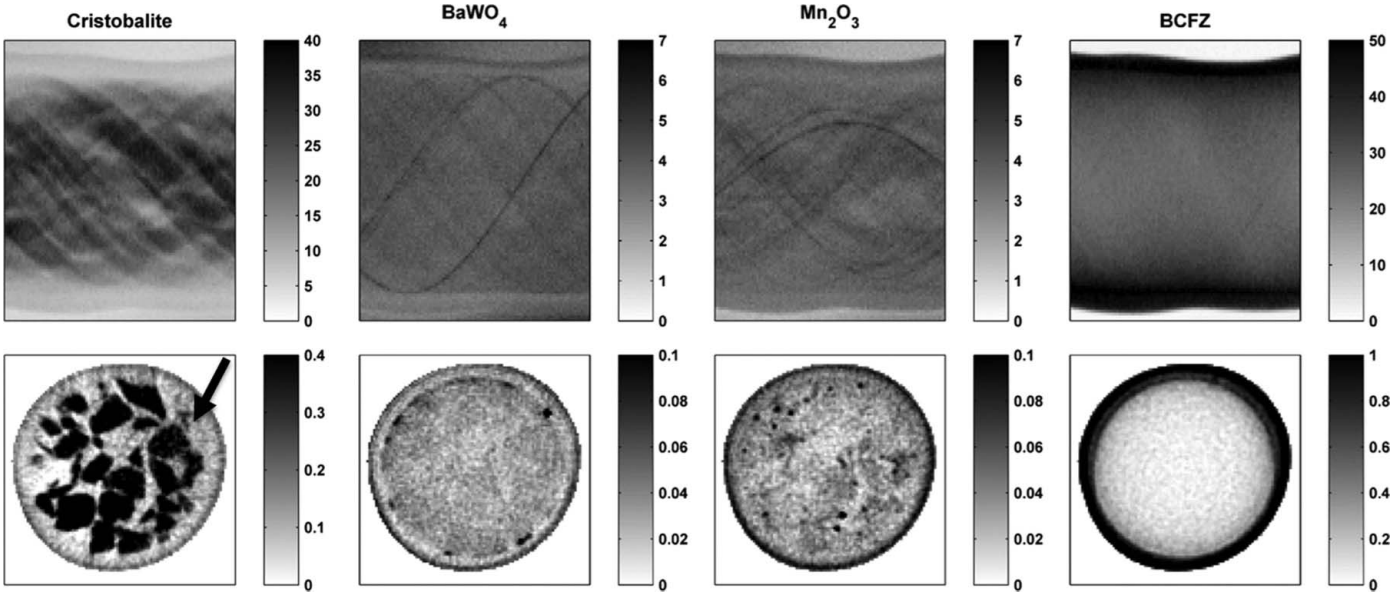

Figure 11
The sinograms of SiO_2 cristobalite, $BaWO_4$, Mn_2O_3 and BCFZ and the corresponding reconstructed XRD-CT images are shown when the median row filter [1 1 1 1 1] is used.

phases. More specifically, these sinograms correspond to scattering angles 4.86, 4.04, 4.56 and 2.87° 2θ, respectively. As expected, when no filter is applied, the spottiness in the original two-dimensional diffraction images is not suppressed and the reconstructed XRD-CT images contain streak artefacts (Fig. 1). As is shown in Fig. 12, all four reconstructed XRD-CT images contain streak artefacts and the desired spatial information is lost.

As the 3% alpha-trimmed-mean filter showed the best performance for removing the single-crystal diffraction artefacts from the XRD-CT data collected with the CMR, this filter was chosen to be tested with the spotty two-dimensional diffraction images of the high-resolution XRD-CT scan. The results after the application of the 3% alpha-trimmed-mean filter are presented in Fig. 13. It can be seen that this filter efficiently removed the artefacts from all the SiO_2 phases and it improved the quality of the reconstructed images corresponding to the Na_2WO_4 phase. The SiO_2 cristobalite and tridymite phases are homogeneously distributed in the three 2%La–2%Mn–1.6%Na–3.1%W/SiO_2 catalyst particles while

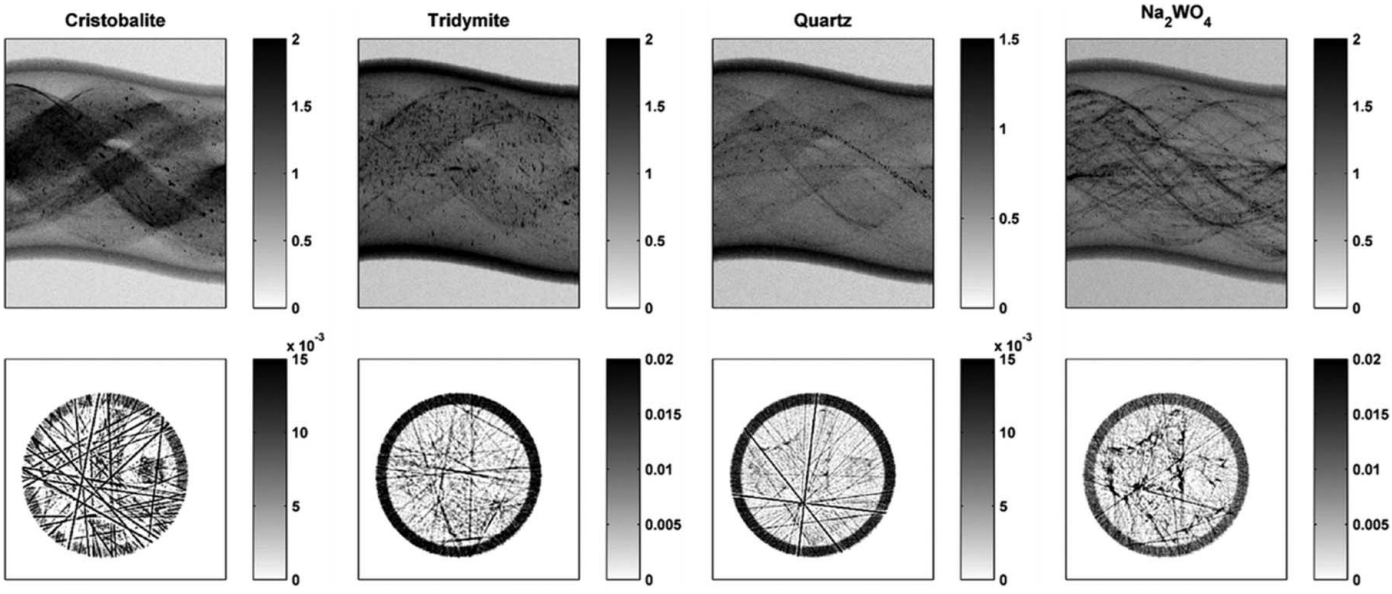

Figure 12
The sinograms of SiO_2 cristobalite, SiO_2 tridymite, SiO_2 quartz and Na_2WO_4 and the corresponding reconstructed XRD-CT images are shown when no filter is used (*i.e.* equivalent to standard azimuthal integration).

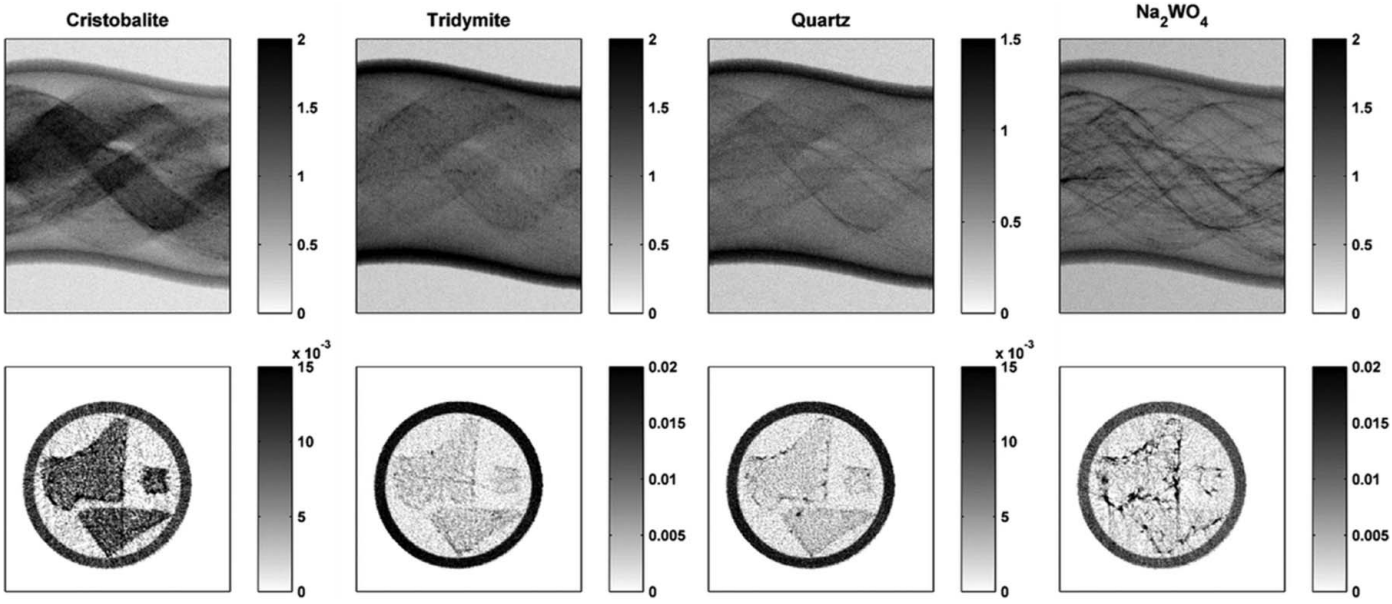

Figure 13
The sinograms of SiO_2 cristobalite, SiO_2 tridymite, SiO_2 quartz and Na_2WO_4 and the corresponding reconstructed XRD-CT images are shown when the 3% alpha-trimmed-mean filter is used.

there are hotspots of the SiO_2 quartz phase. More importantly, the Na_2WO_4 phase is preferentially located near the edge of the catalyst particles.

3.6. Future work

The new filtering approach demonstrated here opens new pathways to improve the quality of the reconstructed XRD-CT images as a variety of different filters can be applied to the polar-transformed images. Filters including the Winsorized mean, the Hampel filter, the modified trimmed-mean filter, local minimum and maximum filters by applying appropriate rank-order filters, local trimmed-mean filters (*i.e.* instead of calculating a single trimmed-mean value for each row in the polar-transformed images), and local mean filters can be tested (Lee & Kassam, 1985; Bednar & Watt, 1984). The effect of adaptive filters, like the adaptive median filter, the adaptive trimmed-mean filter (both symmetrical and unsymmetrical) and their variations, can also be explored (Restrepo & Bovik, 1988; Hsieh, 1994; Taguchi, 1995; Hwang & Haddad, 1995; Marazzi & Ruffieux, 1999; Li *et al.*, 2012). The potential of recently developed arithmetic filters, which avoid the slow process of sorting the values, like the iterative truncated mean, the weighted iterative truncated mean, and the iterative trimmed and truncated mean, should also be investigated (Jiang, 2012; Miao & Jiang, 2013, 2014). However, it is essential to note here that all the filters should fulfil another criterion too: the filtering process must be computationally efficient. This criterion should not be treated lightly as a single XRD-CT scan can easily yield tens of thousands of powder diffraction images.

3.7. Towards high-quality XRD-CT images

The advent of novel, more efficient detectors (*e.g.* the PILATUS3 X CdTe 300K hybrid photon-counting area detector introduced here) along with the continuous effort to achieve more brilliant and intense hard X-rays produced at third-generation synchrotrons (*e.g.* the Upgrade Programme at the ESRF, http://www.esrf.eu/about/upgrade) is expected to set the XRD-CT technique at the forefront of materials science research. XRD-CT has the potential to be used not only for spatially resolved studies but also for dynamic, time-resolved studies leading to five-dimensional (*i.e.* three-dimensional spatial and one-dimensional spectral as a function of time) diffraction imaging (Beale, Jacques *et al.*, 2014). However, this will also lead to a radical increase in the quantity of data being collected during a single beamtime experiment, and efficient, fast and user-friendly routes to yield high-quality, artefact-free XRD-CT images will be needed.

4. Conclusions

We have reported a fast and easy image filtering approach to deal with a common image-based problem during the analysis of XRD-CT data. The formation of spots in the raw two-dimensional diffraction images due to single-crystal effects leads also to hotspots in the sinograms and to line/streak artefacts in the reconstructed XRD-CT images. A potential way to overcome this problem is to apply filters to the original two-dimensional diffraction images after transforming them to polar coordinates. In the future, this simple filtering strategy could also be easily implemented in the Python scripts of *GSAS-II* and *PyFAI* (which can also be used in combination with the *DAWN* software), but also in other software programs used for analysis of XRD-CT data, like *XRDUA*. We compared different filters and showed that the most promising results are generated with a simple alpha-trimmed-mean filter as the streak artefacts can be removed without significant loss of information. This filtering method requires the user to choose a percentage for the trimmed mean and this value is expected to be sample dependent. However, we have shown that the 3% alpha-trimmed-mean shows promising results, even with high-resolution XRD-CT data (*i.e.* beam with a spot size of 2.5×2.5 µm). Future work will focus on the development of a script that can process a single XRD-CT data set efficiently, using several values so that the user can first inspect the quality of the reconstructed XRD-CT images and then choose the correct value and apply it to the rest of the XRD-CT data collected during an experiment.

5. Related literature

For related literature see Middelkoop *et al.* (2014) and Van Noyen *et al.* (2012).

Acknowledgements

The development of the catalysts and membranes for the catalytic membrane reactor used in this work is funded within the DEMCAMER project as part of the European Union Seventh Framework Programme (FP7/2007–2013) under grant agreement No. NMP3-LA-2011-262840. Note: 'The present publication reflects only the authors' views and the Union is not liable for any use that may be made of the information contained therein.' The authors would like to thank the European Synchrotron Radiation Source for beam time, CerPoTech AS for providing the ceramic powders and the Boreskov Institute of Catalysis (BIC) for preparing the catalysts. The authors would also like to thank Dr Pierre Senecal and Dr Stephen Price for assistance during the beamtime. The author SDMJ is supported under the EPSRC RCaH Impact Acceleration Fellowship; AMB and AV are also supported by EPSRC funding. The authors would also like to acknowledge DECTRIS Ltd for providing the PILATUS3 X CdTe 300K hybrid photon-counting area detector for the XRD-CT experiments and Dr Tilman Donath for his assistance with integrating the detector with the ESRF and the discussions regarding the detector's functionalities.

References

Álvarez-Murga, M., Bleuet, P. & Hodeau, J.-L. (2012). *J. Appl. Cryst.* **45**, 1109–1124.

Álvarez-Murga, M., Bleuet, P., Marques, L., Lepoittevin, C., Boudet, N., Gabarino, G., Mezouar, M. & Hodeau, J.-L. (2011). *J. Appl. Cryst.* **44**, 163–171.

Ashiotis, G., Deschildre, A., Nawaz, Z., Wright, J. P., Karkoulis, D., Picca, F. E. & Kieffer, J. (2015). *J. Appl. Cryst.* **48**, 510–519.

Basham, M. *et al.* (2015). *J. Synchrotron Rad.* **22**, 853–858.

Beale, A. M., Gibson, E. K., O'Brien, M. G., Jacques, S. D. M., Cernik, R. J., Michiel, M. D., Cobden, P. D., Pirgon-Galin, Ö., van de Water, L., Watson, M. J. & Weckhuysen, B. M. (2014). *J. Catal.* **314**, 94–100.

Beale, A. M., Jacques, S. D. M., Gibson, E. K. & Di Michiel, M. (2014). *Coord. Chem. Rev.* **277–278**, 208–223.

Bednar, J. B. & Watt, T. L. (1984). *IEEE Trans. Acoust. Speech Signal. Process.* **32**, 145–153.

Bleuet, P., Welcomme, E., Dooryhée, E., Susini, J., Hodeau, J. L. & Walter, P. (2008). *Nat. Mater.* **7**, 468–472.

Bonnin, A., Wright, J. P., Tucoulou, R. & Palancher, H. (2014). *Appl. Phys. Lett.* **105**, 084103.

Bovik, A. C., Huang, T. S. & Munson, D. C. Jr (1983). *IEEE Trans. Acoust. Speech Signal. Process.* **31**, 1342–1350.

Cedola, A., Campi, G., Pelliccia, D., Bukreeva, I., Fratini, M., Burghammer, M., Rigon, L., Arfelli, F., Chang Chen, R., Dreossi, D., Sodini, N., Mohammadi, S., Tromba, G., Cancedda, R. & Mastrogiacomo, M. (2014). *Phys. Med. Biol.* **59**, 189–201.

Davies, L. & Gather, U. (1993). *J. Am. Stat. Assoc.* **88**, 782–792.

De Nolf, W. & Janssens, K. (2010). *Surf. Interface Anal.* **42**, 411–418.

De Nolf, W., Vanmeert, F. & Janssens, K. (2014). *J. Appl. Cryst.* **47**, 1107–1117.

Egan, C. K., Jacques, S. D. M., Di Michiel, M., Cai, B., Zandbergen, M. W., Lee, P. D., Beale, A. M. & Cernik, R. J. (2013). *Acta Biomater.* **9**, 8337–8345.

Elliott, J. C. & Dover, S. D. (1982). *J. Microsc.* **126**, 211–213.

Gordon, R., Bender, R. & Herman, G. T. (1970). *J. Theor. Biol.* **29**, 471–481.

Grunwaldt, J.-D., Wagner, J. B. & Dunin-Borkowski, R. E. (2013). *ChemCatChem*, **5**, 62–80.

Hammersley, A. P. (1998). *ESRF Internal Report.* ESRF, France.

Harding, G., Kosanetzky, J. & Neitzel, U. (1987). *Med. Phys.* **14**, 515–525.

Hounsfield, G. N. (1973). *Br. J. Radiol.* **46**, 1016–1022.

Hsieh, J. (1994). *Proc. SPIE Int. Soc. Opt. Eng.* **2299**, 316–324.

Hwang, H. & Haddad, R. A. (1995). *IEEE Trans. Image Process.* **4**, 499–502.

Jacques, S. D., Di Michiel, M., Beale, A. M., Sochi, T., O'Brien, M. G., Espinosa-Alonso, L., Weckhuysen, B. M. & Barnes, P. (2011). *Angew. Chem. Int. Ed.* **50**, 10148–10152.

Jacques, S. D., Di Michiel, M., Kimber, S. A., Yang, X., Cernik, R. J., Beale, A. M. & Billinge, S. J. (2013). *Nat. Commun.* **4**, 2536.

Jensen, K. M. O., Yang, X., Laveda, J. V., Zeier, W. G., See, K. A., Michiel, M. D., Melot, B. C., Corr, S. A. & Billinge, S. J. L. (2015). *J. Electrochem. Soc.* **162**, A1310–A1314.

Jiang, X. (2012). *IEEE Trans. Image Process.* **21**, 1537–1547.

Kak, A. C. (1979). *Proc. IEEE*, **67**, 1245–1272.

Kak, A. C. & Slaney, M. (1988). *Principles of Computerized Tomographic Imaging.* New York: IEEE Press.

Li, S., Li, Y. & Jin, J. (2012). *J. Syst. Sci. Complex.* **25**, 973–986.

Marazzi, A. & Ruffieux, C. (1999). *Comput. Stat. Data Anal.* **32**, 79–100.

Miao, Z. & Jiang, X. (2013). *IEEE Trans. Signal Process.* **61**, 4149–4160.

Miao, Z. & Jiang, X. (2014). *Signal Process.* **99**, 147–158.

Middelkoop, V., Chen, H., Michielsen, B., Jacobs, M., Syvertsen-Wiig, G., Mertens, M., Buekenhoudt, A. & Snijkers, F. (2014). *J. Membr. Sci.* **468**, 250–258.

Nodes, T. A. & Gallagher, N. C. Jr (1982). *IEEE Trans. Acoust. Speech Signal. Process.* **30**, 739–746.

O'Brien, M. G., Jacques, S. D. M., Di Michiel, M., Barnes, P., Weckhuysen, B. M. & Beale, A. M. (2012). *Chem. Sci.* **3**, 509–523.

Palancher, H., Tucoulou, R., Bleuet, P., Bonnin, A., Welcomme, E. & Cloetens, P. (2011). *J. Appl. Cryst.* **44**, 1111–1119.

Price, S. W. T., Geraki, K., Ignatyev, K., Witte, P. T., Beale, A. M. & Mosselmans, J. F. W. (2015). *Angew. Chem.* **127**, 10024–10027.

Restrepo, A. & Bovik, A. C. (1988). *IEEE Trans. Acoust. Speech Signal. Process.* **36**, 1326–1337.

Stock, S. R. & Almer, J. D. (2012). *J. Appl. Cryst.* **45**, 1077–1083.

Stock, S. R., De Carlo, F. & Almer, J. D. (2008). *J. Struct. Biol.* **161**, 144–150.

Taguchi, A. (1995). *Electronics and Communications in Japan, Part III: Fundamental Electronic Science (English translation of Denshi Tsushin Gakkai Ronbunshi)*, **78**, 46–56.

Toby, B. H. & Von Dreele, R. B. (2013). *J. Appl. Cryst.* **46**, 544–549.

Valentini, L., Artioli, G., Voltolini, M. & Dalconi, M. C. (2012). *J. Am. Ceram. Soc.* **95**, 2647–2652.

Valentini, L., Dalconi, M. C., Parisatto, M., Cruciani, G. & Artioli, G. (2011). *J. Appl. Cryst.* **44**, 272–280.

Vamvakeros, A., Jacques, S. D. M., Middelkoop, V., Di Michiel, M., Egan, C. K., Ismagilov, I. Z., Vaughan, G. B. M., Gallucci, F., van Sint Annaland, M., Shearing, P. R., Cernik, R. J. & Beale, A. M. (2015). *Chem. Commun.* **51**, 12752–12755.

Vanmeert, F., Van der Snickt, G. & Janssens, K. (2015). *Angew. Chem. Int. Ed.* **54**, 3607–3610.

Van Noyen, J., Middelkoop, V., Buysse, C., Kovalevsky, A., Snijkers, F., Buekenhoudt, A., Mullens, S., Luyten, J., Kretzschmar, J. & Lenaerts, S. (2012). *Catal. Today*, **193**, 172–178.

Voltolini, M., Dalconi, M. C., Artioli, G., Parisatto, M., Valentini, L., Russo, V., Bonnin, A. & Tucoulou, R. (2013). *J. Appl. Cryst.* **46**, 142–152.

Wilchinsky, Z. W. (1951). *Acta Cryst.* **4**, 1–9.

Yong Lee, & Kassam, S. A. (1985). *IEEE Trans. Acoust. Speech Signal. Process.* **33**, 672–683.